Ultrafast Electron-Transfer Via Hybrid States at Perovskite/Fullerene Interface

Zhiqiang Guan, Yang Li, Ping Man, Hongji Tan, Qi Wei, Jinjie Liu, Mingjie Li, Thuc Hue Ly, Jun Yin,* and Chun-Sing Lee*

Interfacial charge-transfer between perovskite and charge-transport layers plays a key role in determining performance of perovskite solar cells. The conventional viewpoint emphases the necessity of favorable energy-level alignment of the two components. In recent reports, efficient electron-transfer is observed from perovskite to fullerene-based electron-transport layers even when there are unfavorable energy-level alignments, but the mechanism is still unclear. Here, using an ultrafast in situ two-photon photoelectron spectroscopy, real-time observations of electron-transfer processes at $CsPbI_3/C_{60}$ interface in both temporal and energetic dimensions are reported. Due to strong electronic coupling, a large amount of interfacial hybrid states is generated at the interfaces, aiding fast photoinduced electron-transfer in ≈124 fs. This process is further verified by nonadiabatic molecular dynamics simulations and transient absorption experiments. The short timescale explains why electron-transfer can overcome unfavorable energy-level alignments, providing a guideline for device design.

1. Introduction

Perovskite solar cells are drawing tremendous interest as a promising next-generation photovoltaic technology with a rapidly increasing power conversion efficiency (PCE) exceeding 26%.[1–4]

Z. Guan, Y. Li, P. Man, H. Tan, T. H. Ly, C.-S. Lee
Department of Chemistry
City University of Hong Kong
Hong kong, Hong Kong SAR 000000, P. R. China
E-mail: apcslee@cityu.edu.hk
Z. Guan, Y. Li, P. Man, H. Tan, T. H. Ly, C.-S. Lee
Center of Super-Diamond and Advanced Films (COSDAF)
City University of Hong Kong
Hong kong, Hong Kong SAR 000000, P. R. China
Q. Wei, J. Liu, M. Li, J. Yin
Department of Applied Physics
The Hong Kong Polytechnic University
Hong kong, Hong Kong SAR 000000, P. R. China
E-mail: jun.yin@polyu.edu.hk

Among the state-of-the-art devices, high internal quantum efficiencies approaching unity are achieved, indicating ≈100% charge extraction efficiency from perovskite via charge-transport layers (CTL) and finally collected by electrodes.[5,6] In the conventional viewpoint, such effective charge-transfer from perovskite to CTL requires a favorable energy cascade. In terms of electrons, this means that electrons' transporting energy-level of an electron-transport layer (ETL) is lower than that of perovskite.[7,8] On the other hand, a major factor that currently limits PCE of perovskite solar cells is the mismatch of quasi-Fermi level splitting and open-circuit voltage (V_{OC}).[9,10] The "favorable" energy-level alignment; however, will inevitably cause energy loss when the electron goes down the cascade and also potentially lead to more non-radiative recombination due to back-transfer of electrons, further aggravating this mismatch and reducing V_{OC}.[11]

Theoretically, an ETL with a higher the lowest unoccupied molecular orbital (LUMO) can decrease such V_{OC} loss at the cost of an unfavorable electron-transfer at perovskite/ETL interface. Interestingly, recent reports showed that the unfavorable energy barriers seem not to weaken charge extraction ability, which is somewhat counterintuitive because the electron-transfer rate should be very sensitive to the energy barrier due to its exponential relationship with the barrier height.[12] For example, Wolff et al. compared fullerene and its derivatives as ETLs. They found that the solar cell using indene-C_{60}-trisadduct, whose LUMO was 0.64 eV higher than conduction band minimum (CBM) of perovskite, showed a comparable short-circuit current (J_{sc}) with the device using C_{60}, whose LUMO was 0.21 eV lower than perovskite's CBM.[13] This similar electron extraction was attributed to the fullerene derivatives' LUMO tail states down to the perovskite's CBM. Similarly, Xue reported that a device using another fullerene derivative of 56π-electron dihydromethano/indene fullerene, whose LUMO was 0.24 eV higher than CBM of perovskite, kept the same J_{SC}; while, delivering a higher V_{OC}. They attributed the improvement of device performance to the passivation effect.[14] In addition, Hu et al. demonstrated that by using a fullerene derivative of indene-C_{60}-propionic acid hexyl ester (IPH), whose LUMO was 0.2 eV higher than the CBM of perovskite, both V_{OC} and J_{SC} could be enhanced simultaneously. The authors attribute the improvement of charge

ADVANCED
SCIENCE NEWS

www.advancedsciencenews.com

ADVANCED
MATERIALS

www.advmat.de

extraction to an improved electron mobility and smaller electron capture radius of IPH.[15] This effective charge extraction was also observed in perovskite/inorganic ETL interface. For example, Ding et al. observed an efficient electron-transfer from perovskite to ZnO with higher CBM of 0.2 eV. It is suggested that some shallow defect states in ZnO layer can provide additional pathways for charge transfer.[16] These results show that energy barriers of ≈ 0.2–0.3 eV have no obvious adverse effect on electron extraction from perovskite to ETLs. This implies that other than the energy-level alignment, there should be additional factors dominating the charge-transfer process at perovskite/CTL interfaces. Up till now, it is still not clear how such "unfavorable" energy-level alignment can be overcome to achieve the observed effective charge-transfer.

Here, by combining time-resolved spectroscopic techniques and theoretical approaches, we probe the electron-transfer process at the interface between an all-inorganic perovskite of cesium lead iodide ($CsPbI_3$) and a common-used ETL of C_{60} with an "unfavorable" energy-level alignment. Experimentally, we use ultrafast in situ two-photon photoelectron spectroscopy (2PPE) to track the electron dynamics in both energetic and temporal dimensions. Interestingly, we find that there exists strong interfacial hybrid states through which photo-generated electrons in $CsPbI_3$ can swiftly transfer to C_{60} with a time constant of ≈ 124 fs. Theoretically, we carry out density functional theory (DFT) calculations to locate the interfacial hybrid state originating from the electronic coupling between $CsPbI_3$ and C_{60}. The ultrafast process observed in the 2PPE experiments is consistent with simulation results from nonadiabatic molecular dynamics (NAMD) and experimental results from transient absorption (TA) spectroscopy. We relate the efficient charge-carrier extraction across energy barrier to this short electron-transfer timescale, which results from the strong electronic coupling effect. The revealed mechanism provides a guideline for designing high-performance perovskite solar cells.

2. Results and Discussion

The $CsPbI_3/C_{60}$ pair is used here as a prototypical perovskite/ETL system. Both materials are prepared in an ultra-high vacuum environment in order to keep a "clean" surface. A 20 nm $CsPbI_3$ film is first prepared using a dual-source co-evaporation method (see Experimental Section). X-ray diffraction result shows that the $CsPbI_3$ is a γ-phase and orthorhombic crystal system (Figure S1a, Supporting Information).[17] Its optical bandgap is estimated to be 1.75 eV according to the tauc plot (Figure S1b, Supporting Information). Considering the exciton binding energy of $CsPbI_3$ is $\approx$ 20 meV, we calculate its electronic energy gap (E_g) to be $\approx$ 1.77 eV.[18] C_{60} of different thicknesses is then deposited step-wise onto the $CsPbI_3$ film. Absorption, atomic force microscopy, and X-ray photoelectron spectroscopy results indicate successful deposition of C_{60} layer on $CsPbI_3$ (Figures S1–S3, Supporting Information). Stable core-level peaks of Cs, Pb, and I elements also demonstrate that the deposition of C_{60} does not induce chemical change on the $CsPbI_3$.

For perovskite/C_{60} system, in some literatures, the typical $CH_3NH_3PbI_3/C_{60}$ combination is described as a type-II heterojunction with the LUMO of C_{60} lower than the CBM of

$CH_3NH_3PbI_3$.[19,20] On the other hand, some photoelectron spectroscopic experiments demonstrate that the LUMO of C_{60} is very close or even higher than the CBM of some perovskites, suggesting that actual interfaces vary depending on different preparing methods, terminations, and components.[21–24] To observe electronic structures of our $CsPbI_3/C_{60}$ system, in situ ultraviolet photoelectron spectroscopy (UPS) is carried out on the systems with C_{60} thicknesses of 0, 2, 4, 10, and 20 Å, respectively. It has been reported that due to the low density of states (DOS) at valence band maximum (VBM) of perovskite, specific analysis on UPS data is required to accurately find the energy position.[25] The background from the satellite emission is first subtracted from experimental data according to ref. [26]. Second, to extract the individual energy edge from the combined bilayer, a global fitting method is applied (Figure S4 and Note S1, Supporting Information). The obtained energy-level diagram is shown in **Figure 1a**. Vacuum-levels of $CsPbI_3$ and adjacent C_{60} layer present negligible difference, indicating a vacuum-level alignment condition (Figure S5, Supporting Information). As for the increase of C_{60} thickness, the energy levels slightly upshift, suggesting the electron-transfer from $CsPbI_3$ to C_{60}. Based on the E_g of $CsPbI_3$ and C_{60} (E_g = 2.3 eV),[21] the CBM of $CsPbI_3$ and the LUMO of 2 Å C_{60} layer can be determined, respectively as 0.2 and 0.33 eV above Fermi level (E_f). This means that a 0.13 eV electron extraction barrier exists from $CsPbI_3$ to C_{60}, which is an unfavorable energy-level alignment but suitable for our study.

A commonly used experiment for verifying the occurrence of charge-transfer process is the quench of photoluminescence (PL) intensity when perovskite is attached with a CTL layer.[27,28] Figure 1b shows the PL spectra of pure $CsPbI_3$ and $CsPbI_3/C_{60}$ bilayers. The $CsPbI_3$ film exhibits an obvious PL peak at 700 nm, corresponding to the E_g of 1.77 eV. Upon deposition of C_{60}, this peak is strongly quenched, indicating the efficient charge transfer. The PL spectra with longer excitation wavelength of 550 nm is exhibited in Figure S6, Supporting Information for comparison. Similar quenching can be observed, proving the occurrence of charge-transfer.

Another method to check this process is to observe the lifetime of charge carriers in perovskite using time-resolved PL (Figure 1c).[28,29] The charge-transfer provides an additional decay route for charge carriers in perovskite in addition to typical trap-induced and bimolecular recombination,[30] leading to the decrease of PL lifetime. Figure 1c compares the charge carriers' lifetimes of $CsPbI_3$ and $CsPbI_3/C_{60}$ bilayer with a probe wavelength of 700 nm. It clearly shows that the average lifetime of charge carriers decreases from 182.6 ns for pure $CsPbI_3$ to 23.9 ns for $CsPbI_3/C_{60}$ bilayer, evidencing the occurrence of electron-transfer (Table S1, Supporting Information).

To investigate why electrons can effectively transfer under unfavorable energy-level alignment condition between $CsPbI_3$ and C_{60}, we next apply an ultrafast in situ 2PPE technique, which allows us to probe the electron-transfer process in both energetic and temporal dimensions.[31,32] Measured samples are either pure $CsPbI_3$ or $CsPbI_3/C_{60}$ films with different C_{60} thickness. A schematic for the 2PPE experimental is provided in Figure S7, Supporting Information. First, a laser with 1.88 eV photon energy is used to excite samples, pumping an electron from valence band into unoccupied conduction band in $CsPbI_3$.
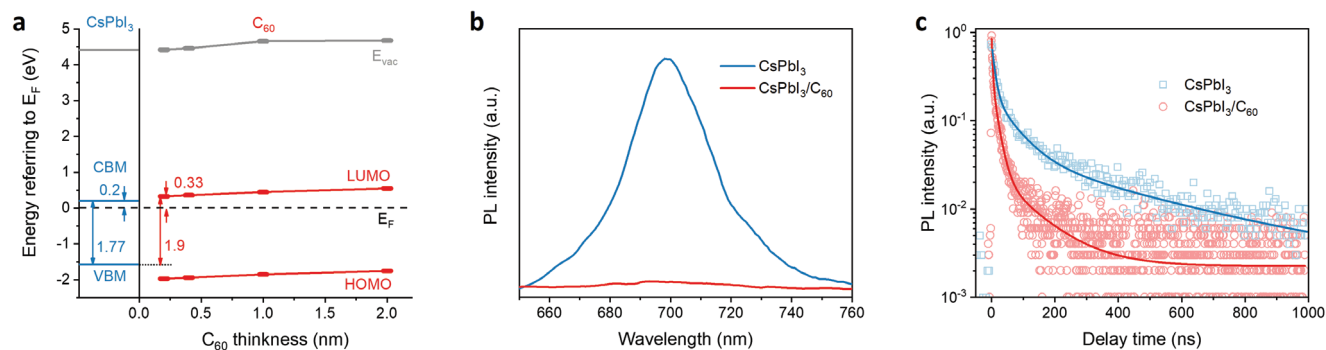
Figure 1. Electronic structure and charge-transfer of $CsPbI_3$/C_{60} heterojunction. a) Energy level diagram of $CsPbI_3$/C_{60} heterojunction. The bandgap of $CsPbI_3$ is 1.77 eV. The energy difference between CBM and E_F is 0.2 eV. For C_{60}, the energy difference between LUMO and E_F is 0.33 eV, meaning that the LUMO of C_{60} is 1.9 eV higher than VBM of $CsPbI_3$. With increasing the C_{60} thickness, energy levels slightly upshift. b) PL spectra of pure $CsPbI_3$ film and $CsPbI_3$/C_{60} bilayer. c) Time-resolved PL of pure $CsPbI_3$ film and $CsPbI_3$/C_{60} bilayer.

The reason for selecting this photon energy is to guarantee that the probed electrons are only from $CsPbI_3$ rather than from C_{60} because 1.88 eV is higher than the E_g of $CsPbI_3$, but lower than that of C_{60}. Subsequently, with a well-defined delay time, a second laser with photon energy of 4.59 eV is used to ionized the excited electron; and then, the energy of the photoelectron can be detected by an energy analyzer.

Figure 2a shows a pseudo-color plot of a 2PPE spectrum of a pure $CsPbI_3$ film. The y-axis displays the energy of excited electrons referring to the perovskite's VBM. Upon excitation ($\approx$0 ps), there generates a feature with a peak around 1.9 eV, which is attributed to electrons in conduction band. This energy also corresponds to the pump photon energy of 1.88 eV. The electrons then slightly relax into lower-energy states via a "cooling" process; and then, exist as "cooled" electrons (Figure S8, Supporting Information).[33,34] It should be noted that in our experiment, due to the low pump photon energy (0.11 eV above CBM), the electrons that we excite are not very "hot," which is evidenced as a slight decrease of the calculated average excess energy of the electrons (Figure S9, Supporting Information).[33] The selection of this photon energy aims to simulate the charge carrier collection process in actual device because most carriers reaching the perovskite/CTL interface through drift and diffusion processes should be already cooled.[35] To distinguish the electronic dynamics in $CsPbI_3$, we carry out a global analysis method on the 2PPE results (Note S2, Supporting Information). The 2PPE spectrum can be successfully fitted using a sequential model with two components (Figure S10, Supporting Information). The normalized evolution associated spectra (EAS) are shown in Figure S11, Supporting Information. A high-energy component with a peak at 1.9 eV is attributed to hot electrons, and a low-energy counterpart with a peak at 1.82 eV can be assigned to cooled electrons.

To illustrate this cooling process, we show a spectral evolution in Figure 2b by presenting spectral profiles at delay times of 0, 140, 340, and 540 fs, respectively. Each spectrum can be expressed as a combination of two EAS. For 0 fs, pump photons create 74.4% hot electrons and 25.6% cooled electrons. With time delaying, the ratio of hot electrons gradually reduces, together with an increase of cooled electrons. When the delay time exceeds 500 fs, the hot electrons component becomes negligible, indicating the completion of the cooling process. Meanwhile, the

whole spectral profile changes with a slight shift from high to low energy region, which is ascribed to bandgap renormalization effect.[34,36] Figure 2c shows the electronic kinetics with electron energies of 1.99 (red circle) and 1.69 eV (blue triangle), which are, respectively selected to represent the hot and cooled electrons. In addition, concentration decay profiles (solid lines) obtained from global analysis are also shown for comparison. The concentration decay profiles show good fit with 2PPE data, indicating the rationality of the fitting model. The sequential kinetics clearly demonstrate the relaxation process of excited electrons from hot to cooled states, with a transfer rate of 5.41 ps^{-1} (Table S2, Supporting Information). The corresponding transit time; thus, is regarded as the relaxation time (τ_{relax} = 184.8 fs) of hot electrons in $CsPbI_3$ for this experimental condition.

We next probe the interfacial electron-transfer by depositing a 0.25 monolayer (ML) of C_{60} (interlayer distance of 8.17 Å is used) on top of the $CsPbI_3$ film.[37] From the 2PPE plot of Figure 2d, we surprisingly observe a new spectral feature upon excitation with energy higher than probed hot electrons of pure $CsPbI_3$. As marked with a pink triangle, this feature locates at the energy around 2.1 eV above the VBM of $CsPbI_3$. To probe the origin of this feature, we present the 2PPE spectra at 0, 60, 120, and 500 fs in Figure 2e and fit the spectra with individual Gauss peak for different components. For simplifying the fitting procedure, components of hot and cooled electrons of $CsPbI_3$ are combined together as the total DOS profile (blue region). For 0 fs, in addition to the $CsPbI_3$'s profile, a peak (pink) appears upon pumping at higher energy region than $CsPbI_3$ with its center at 2.0 eV. As time develops to 500 fs, this peak gradually diminishes and the spectrum is dominated by $CsPbI_3$'s DOS again (Figure S12, Supporting Information). As the central energy of pump photons (1.88 eV) is lower than the E_g of C_{60}, we rule out the possibility that this feature originates from the HOMO-to-LUMO excitation of C_{60}. As the 2PPE technique predominately probes the topmost surface,[38] the surface with such a thin and discontinuous C_{60} film (Figure S2, Supporting Information) can be specifically regarded as the $CsPbI_3$/C_{60} interface. According to literature, there exists a wavefunction hybridization at the perovskite/fullerene interface.[24,39] We thus speculate that the origin of this high-energy feature may be from C_{60}'s LUMO or interfacial hybrid states.
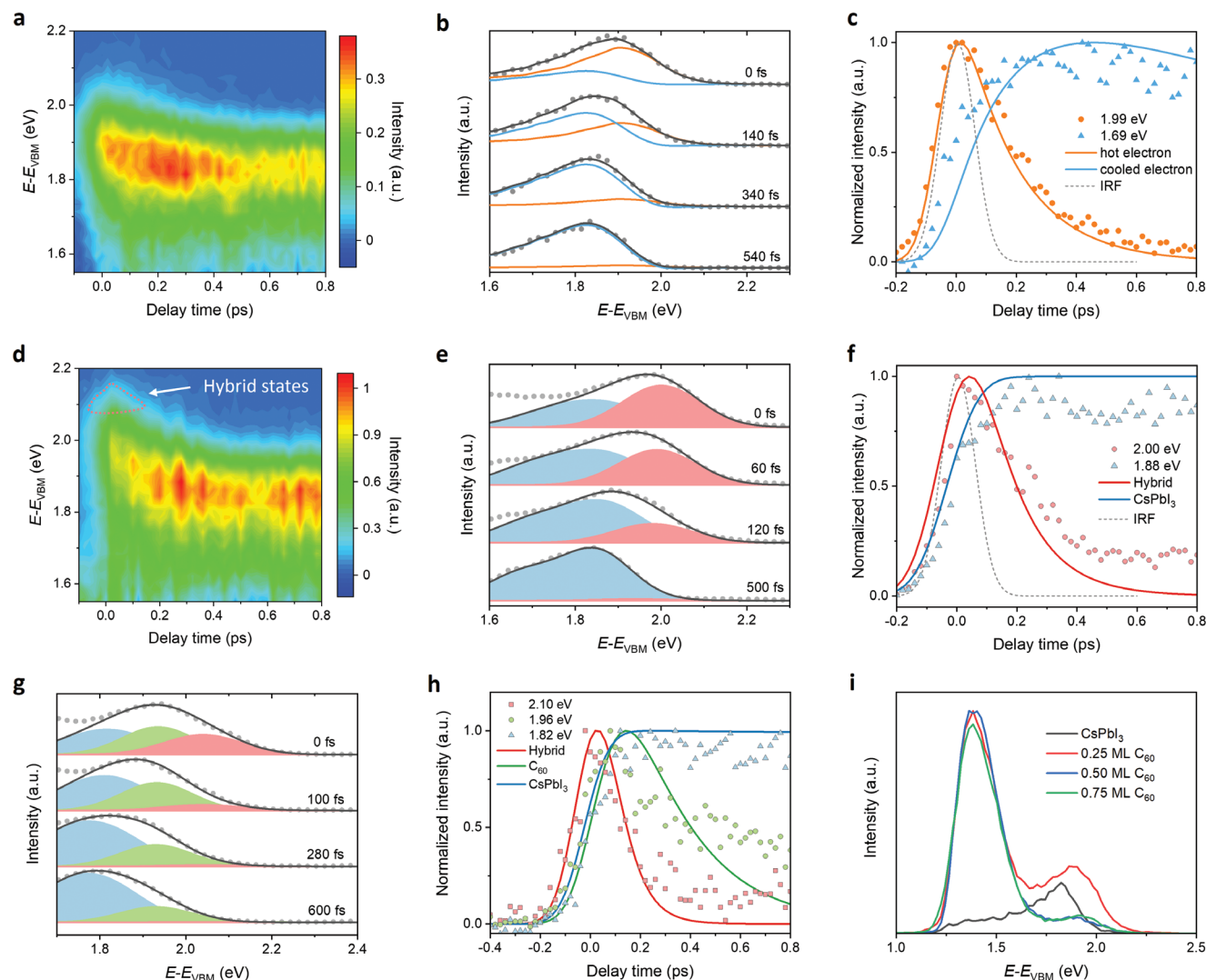
ADVANCED
SCIENCE NEWS

www.advancedsciencenews.com

ADVANCED
MATERIALS

www.advmat.de

Figure 2. Electron-transfer process at $CsPbI_3/C_{60}$ interface. a) Pseudo-color plot of 2PPE spectrum of pure $CsPbI_3$ film. b) Spectral evolution and global fitting of pure $CsPbI_3$ for delay times of 0, 140, 340, and 540 fs. c) Kinetics for hot (1.99 eV) and cooled (1.69 eV) electrons of pure $CsPbI_3$. d) 2PPE pseudo-color plot of $CsPbI_3/0.25$ ML C_{60} film. e) Spectral evolution of $CsPbI_3/0.25$ ML C_{60} film for delay times of 0, 60, 120, and 500 fs. f) Kinetics of hybrid states (2.00 eV) and $CsPbI_3$ (1.88 eV). g) Spectral evolution of $CsPbI_3/0.5$ mL C_{60} film for delay times of 0, 100, 280, and 600 fs. h) Kinetics of hybrid states (2.10 eV), C_{60} (1.96 eV), and $CsPbI_3$ (1.82 eV). i) 2PPE spectral profiles for different samples recorded at 80 fs without removing spectral feature before time zero. For kinetic plot (c,f,h), symbols are 2PPE data and solid lines are fitting from global and target analysis.

Figure 2f shows electron kinetics with energies of 2.00 and 1.88 eV, which we select to represent the high-energy feature and total $CsPbI_3$s DOS, respectively. The generation of 2.00 eV signal is very fast, displaying almost the same rising trend with instrument response function (IRF). We thus apply a parallel model in the global analysis to fit this kinetics by assuming two components, that is, high-energy feature (red curve) and $CsPbI_3$ (blue curve) (Figure S11, Supporting Information). The profiles of two associated spectra show similar shapes with the fitting Gauss peaks in Figure 2e, indicating the validity of our fitting method. Good fit can also be found between concentration decay profiles and experimental data in kinetics. Simultaneous appearance of this high-energy feature upon excitation basically rules out the possibility that it is from C_{60}'s LUMO due to the very short timescale.[31] We thus assign it to the hybrid states at the

interface between $CsPbI_3$ and C_{60} and will discuss it below. The delay time between the peak of IRF and that of the concentration decay profile of hybrid states, ≈ 32 fs, is estimated as the transfer time constant. The slow rising kinetics of $CsPbI_3$ is because it is a combination of both hot and cooled electrons.

We then further increase C_{60}'s thickness to 0.5 and 0.75 mL to track the electron-transfer across the interface. Figure 2g shows 2PPE spectral evolution of $CsPbI_3/0.5$ ML C_{60}. For the spectrum at 0 fs, in addition to hybrid states' and $CsPbI_3$'s DOS distributions obtained above, there obviously appear a new peak (green) centered at 1.93 eV (1.97 eV for 0.75 ML, Figures S13 and S14, Supporting Information). Referring to the energy diagram in Figure 1a that the LUMO level of C_{60} is 1.9 eV higher than the VBM of $CsPbI_3$, we thus ascribe this new peak to the electron distribution of C_{60}'s LUMO. The slight increase of peak

2407406 (4 of 10)

**ADVANCED
SCIENCE NEWS**

www.advancedsciencenews.com

**ADVANCED
MATERIALS**

www.advmat.de

energy from 1.93 to 1.97 eV for 0.5 to 0.75 ML is also consistent with the increase of LUMO energy for thicker C_{60} layer. With increasing delay time, the profiles of interfacial hybrid states and $CsPbI_3$'s DOS fundamentally show similar trends with those of 0.25 mL C_{60} sample. On the other hand, the peak of C_{60}'s LUMO can still persist for 600 fs, which is much longer than hybrid states, indicating they are from different origins. The generation and decay tendencies can be more clearly observed in electron kinetics of Figure 2h. The electron energies of 2.10, 1.96, and 1.82 eV are used to represent the interfacial hybrid states, C_{60}'s LUMO, and $CsPbI_3$'s CBM, respectively. Similar to the 0.25 mL C_{60} sample, signals of hybrid states appear very fast. Then, the signals of C_{60}'s LUMO rise, clearly showing a time delay after hybrid states. To fit the dynamics, we carry out a target analysis by assuming the hybrid states and $CsPbI_3$ as initial states and C_{60} as a product of hybrid states (Note S2, Supporting Information). The 2PPE spectra and kinetics can be successfully fitted with this model, proving the validity of our assignment on these peaks. The rising time constant (τ_{rising}) of the C_{60} LUMO signal is 124 fs, which is estimated as the electron-transfer time from $CsPbI_3$ to C_{60}. This phenomenon can also be observed in the 0.75 mL C_{60} sample, which shows a more pronounced C_{60} LUMO component than hybrid states and $CsPbI_3$'s CBM because the $CsPbI_3/C_{60}$ interface is further away from the topmost surface for the thicker C_{60} layer (Figure S13, Supporting Information). The appearance of a new C_{60} peak in 0.5 and 0.75 mL C_{60} samples and the electron-transfer dynamics between hybrid states and C_{60} also verify our assumption that high-energy feature originates from interfacial hybrid states.

This ultrafast electron-transfer in a timescale around a hundred fs has not been reported in perovskite/fullerene systems. As mentioned in Introduction part, for this kind of system, the existence of energy barriers with hundreds meV seems not to weaken the electron-extraction capability. It is noteworthy that the electron-transfer efficiency is determined not only by energy-level alignment but also by electronic coupling strength between molecular orbitals or energy bands.[37] Figure 2i presents the 2PPE spectra of different samples recorded at 80 fs without removing spectral feature before time zero. A high peak at 1.38 eV for samples with C_{60} is ascribed to triplet states of C_{60} due to their long lifetime.[38] Clearly, for the 0.25 mL C_{60} sample, the hybrid states' spectral profile ranging from 1.7 to 2.2 eV is higher than the $CsPbI_3$'s conduction band and much higher than C_{60}'s LUMO. As 2PPE intensity directly reflects the population of electrons at the topmost surface,[31] the large spectral profile specifies a great number of hybrid states distributing at the interface, implying strong electronic coupling between $CsPbI_3$ and C_{60}. This coupling effect allows photo-generated electrons in CBM of $CsPbI_3$ ultrafast transferring to C_{60}'s LUMO via interfacial hybrid states by overcoming the unfavorable energy-level alignment. We therefore reasonably relate the high electron-extraction efficiency in devices to this ultrafast electron-transfer timescale, which is finally attributed to the strong hybridization effect between perovskite and fullerene.

For the nature of interfacial hybrid states, we attribute them to the wavefunction mixing of the conduction band of perovskite and LUMO of C_{60}. This hybridization phenomenon has also been observed for different heterojunction systems. For example, Caplins et al. observed a hybrid state resulting from the interaction between the unoccupied molecular states of the phthalocyanine (Pc) ligand and the Shockley surface state of Ag at $H_2Pc/Ag(111)$ surface.[40] Grancini et al. calculated the interfacial hybridized excited states at organic/organic system.[41] Virgili et al. reported that the hybridization of the HOMO of poly(p-styrenesulphonic acid) and valence band of CdSe facilitated interfacial charge separation.[42] In addition, Kelly et al. observed hybridization at the C_{60} and ZnO interface. The authors attributed it to the mixing molecular wavefunction with localized components of ZnO band structure.[43] These reports indicated that hybridization is a general phenomenon in heterojunctions involving organic and inorganic semiconductors as well as metals. The major difference is the electronic states that take part in hybridizing process.

Aiming to further verify that the high-energy feature originates from hybridization effect between $CsPbI_3$ and C_{60}, we carry out a control experiment by replacing C_{60} with a wide bandgap molecule of 1,4-Bis(triphenylsilyl)benzene (UGH-2). The HOMO and LUMO of UGH-2 are 7.2 and 2.8 eV, respectively, meaning that $CsPbI_3$/UGH-2 is a type I heterojunction, with LUMO of UGH-2 much higher than CBM of $CsPbI_3$[44] (Figure S15a, Supporting Information). Thus, at the characterized energy range (i.e., ≈1.8–2.1 eV above VBM of $CsPbI_3$), there should be no molecular orbital for UGH-2 to interact with $CsPbI_3$ and neither is a high-energy feature. This is exactly what we observed in 2PPE results in Figure S15, Supporting Information, which show similar spectra and kinetics with pure $CsPbI_3$.

To gain insight into the orbital hybridization and electron-transfer process, we conduct DFT calculations and NAMD simulations.[45–47] **Figure 3a** shows the optimized interfacial structure of $CsPbI_3/C_{60}$ system ($CsPbI_3$ is in orthorhombic γ-phase with a CsI-rich termination). Figure 3b presents the calculated energy levels together with electron-transfer process (left) and electronic charge densities (right) for $CsPbI_3$, C_{60}, and $CsPbI_3/C_{60}$ heterojunction. Considering the pump photon energy and bandgap of $CsPbI_3$ in our experiments, we focus on the hot electron at CBM + 3 level (i.e., ≈0.3 eV above CBM). Our calculations reveal the emergence of a new interfacial state at the energy level higher than both the CBM of $CsPbI_3$ and the LUMO of C_{60}, indicating orbital hybridization at the top surface of $CsPbI_3$ (marked by a red circle in Figure 3b). This finding aligns with observations from the spectral evolution in our 2PPE experiments. The excited hot electrons in CBM + 3 of $CsPbI_3$ may experience two processes: cooling to CBM or electron-transfer to interfacial hybrid state. Figure 3c compares the time evolution of these two processes using NAMD simulations, which show a more rapid decay in charge population for electron-transfer compared to hot-electron cooling. The time constants (time at 1/e position) are 55.7 fs for electron-transfer and 153.8 fs for hot-electron cooling, consistent with the values obtained from 2PPE experiments.

The results of in situ 2PPE experiments and theoretical calculations provide a real-time observation of electron-transfer process from perovskite to fullerene in both temporal and energetic dimensions. As illustrated in **Figure 4**, for pure $CsPbI_3$, the photo-generated electrons near conduction band edge will relax into CBM at ≈185 fs. When $CsPbI_3$ is attached with C_{60}, hybrid states generate at the interface due to electronic coupling. Electrons thus can ultrafast transfer to the hybrid states in ≈32 fs and further to the LUMO of C_{60} in ≈124 fs. The almost
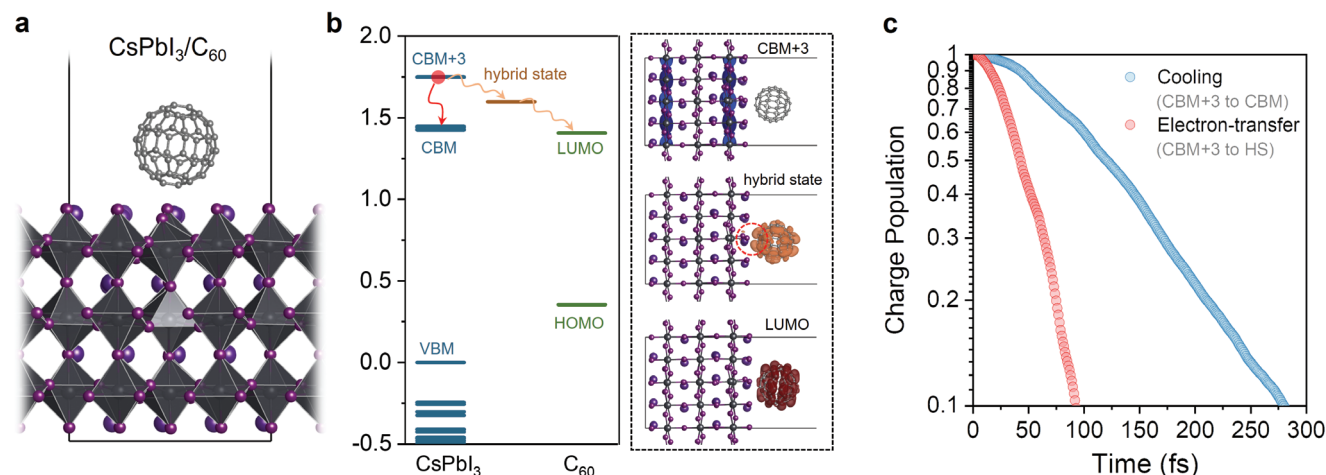
**ADVANCED
SCIENCE NEWS**

www.advancedsciencenews.com

**ADVANCED
MATERIALS**

www.advmat.de

Figure 3. NAMD calculations. a) Optimized crystal structure of CsPbI$_3$/C$_{60}$ heterojunction. b) Calculated energy levels and electronic charge densities for CBM + 3 of CsPbI$_3$, hybrid state (marked in a red circle) and LUMO of C$_{60}$. c) Time evolution of hot-electron cooling from CBM + 3 to CBM in CsPbI$_3$ and electron-transfer from CBM + 3 of CsPbI$_3$ to hybrid state (HS). All calculations were performed at the GGA/PBE+SOC level.

simultaneous rise of hybrid states and CsPbI$_3$ excited states suggest a coherent resonance scenario,[31] leading to a total time of electron-transfer comparable or even shorter than the hot-electron cooling process inside perovskite itself. This short timescale allows electrons in perovskite efficiently transferring into adjacent ETL molecules, consequently achieving a high internal quantum efficiency for perovskite solar cells. It should be mentioned that due to the spectral width of the pump laser, small number of hot electrons inevitably generate with excess energy of ≈0.2–0.3 eV. This is why the hot electron behaviors, that is, relax-

Figure 4. Energy diagram describing photo-generated electron-transfer process across CsPbI$_3$/C$_{60}$ interface. Upon excitation with energy above bandgap, a hot-electron is generated in the conduction band of CsPbI$_3$ with excess energy. The hot-electron will relax into CBM in ≈185 fs; and then, slowly decay back to valence band. Once attached with C$_{60}$, hybrid states generate at CsPbI$_3$/C$_{60}$ interface due to electronic coupling. The excited electron thus can transfer to hybrid states in ≈32 fs or further to LUMO of C$_{60}$ in ≈124 fs.

ation and electron-transfer, are involved in our experiments and calculations. However, the hot-electron transfer is not considered to be a main route under the current experimental conditions due to the small number of hot-electrons as confirmed by the stable average excess energy (Figure S9, Supporting Information). In addition, we would like also to emphasize that there should be a range of barrier height for this efficient charge-transfer. Beyond this range, the charge-transfer would still be impeded.

As a complementary ultrafast optical technique, TA is next applied to confirm the observed interfacial electron dynamics. **Figure 5a** shows time-resolved TA spectra for pure CsPbI$_3$ at delay times from 0 to 511 fs. The energy density is as low as 0.15 µJ cm^{-2}. The peak ranging from 650 to 720 nm can be assigned to the bleaching signal of CsPbI$_3$.[48] With time evolution, it clearly presents a relaxation process as the peak position shifts from short to long wavelengths.[49,50] This phenomenon is more pronounced in kinetic profiles (Figure 5c), in which hot and cooled electrons (664 and 695 nm, respectively) show an obvious transition trend at the initial hundreds of fs.

For TA measurement on CsPbI$_3$ (20 nm)/C$_{60}$ (20 nm) heterojunction, due to the low energy density of pump light, we can individually study the bulk or interfacial characteristics by selectively illuminating the heterojunction from either CsPbI$_3$ or C$_{60}$ side. For the illuminating direction from CsPbI$_3$ side, which mainly reflects bulk characteristics of CsPbI$_3$ because of its relatively high thickness of 20 nm, bilayer sample shows no significant difference in spectral profiles (Figure S16, Supporting Information) with pure CsPbI$_3$ but exhibits faster decay trace of bleaching signals for both hot and cooled electrons (Figure 5c), proving the existence of electron-transfer.[50] On the other hand, for illuminating from C$_{60}$ side (20 nm), as shown in Figure 5b, the time-resolved spectral profiles show a much different changing trend, that is, the bleaching peak first appears at the low energy (long wavelength) region; then, gradually recovers to the broad peak profile like pure CsPbI$_3$. For kinetics, different from the pure CsPbI$_3$ and the heterojunction illuminated from CsPbI$_3$ side, there is no obvious transition tendency between hot and cooled electrons at the initial rising stage. On the contrary, TA
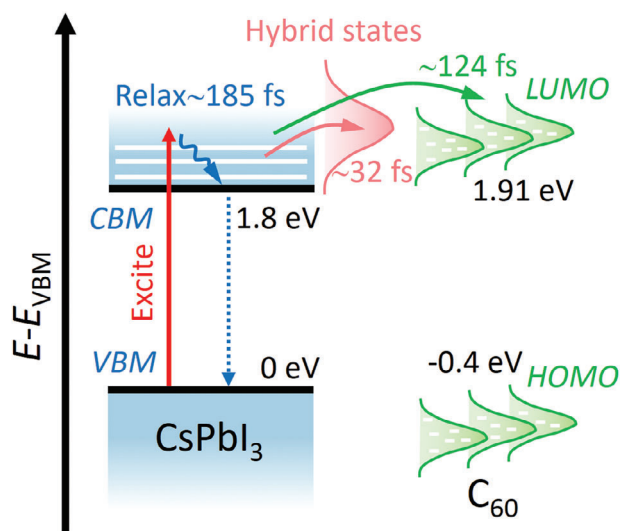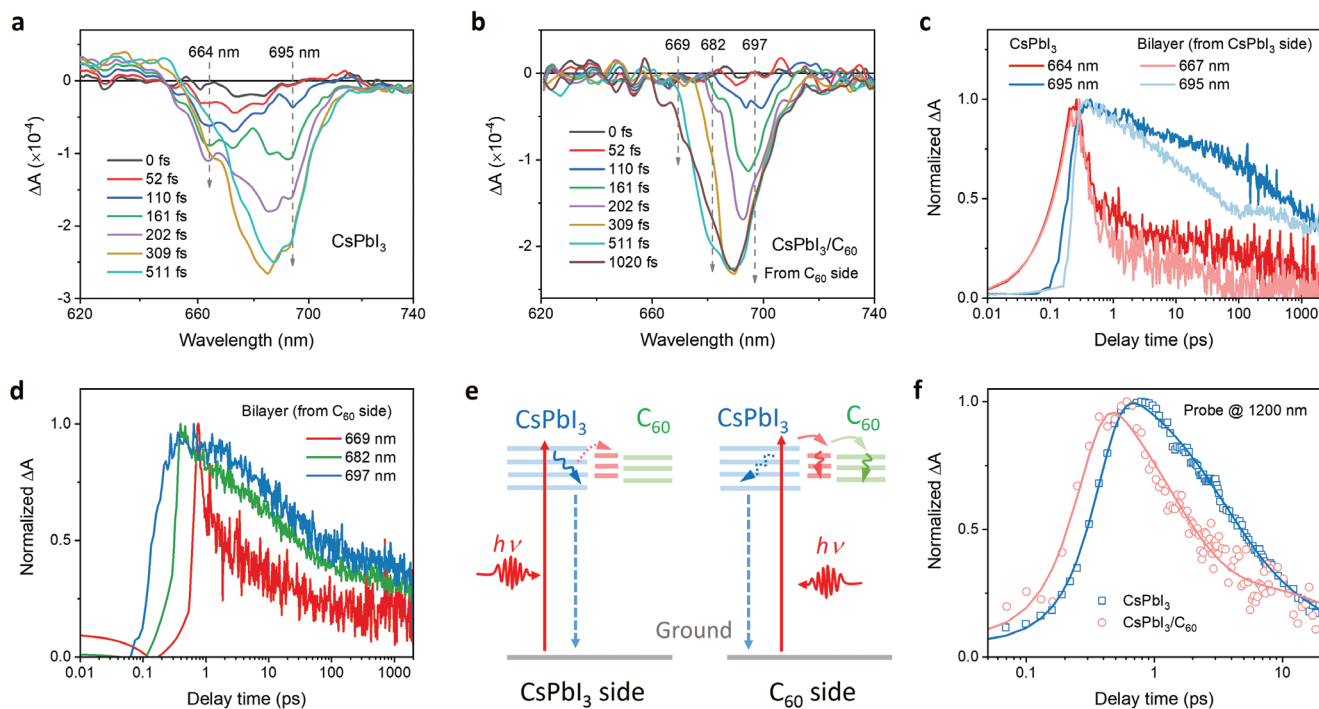
**ADVANCED
SCIENCE NEWS**

www.advancedsciencenews.com

**ADVANCED
MATERIALS**

www.advmat.de

Figure 5. Electron-transfer dynamics in TA characterization. a,b) TA spectra of pure CsPbI$_3$ (a) and CsPbI$_3$/C$_{60}$ (b) films at different delay times. Arrows indicate the wavelength of hot and cooled electrons used for kinetic studies. For CsPbI$_3$/C$_{60}$ film, the excitation light illuminates the heterojunction from C$_{60}$ side for investigating the interfacial condition. c) TA kinetics of hot and cooled electrons of pure CsPbI$_3$ and CsPbI$_3$/C$_{60}$ bilayer, in which the illumination is from CsPbI$_3$ side. d) TA kinetics of CsPbI$_3$/C$_{60}$ bilayer with illumination from C$_{60}$ side. e) Schematics illustrating the electron dynamics observed for different illumination directions. Left: from CsPbI$_3$ side. Right: from C$_{60}$ side. f) TA kinetics for the signals probed at wavelength of 1200 nm. The pump wavelength is 660 nm, same with 2PPE experiment.

signals of cooled electrons (697 nm) generate at first. Afterward, the signals of hot electrons rise with hundreds of fs delay (Figure 5d). As the pump photon energy is lower than the bandgap of C$_{60}$, we can rule out influence from C$_{60}$ layer. Therefore, the change of the bleaching signal at this situation should originate from the difference of excited electrons in CsPbI$_3$, and specifically, at the CsPbI$_3$/C$_{60}$ interface.

The mechanism can be explained as a schematic illustrated in Figure 5e. For the illumination direction from CsPbI$_3$ side (left), the excited position is near the bottom surface of CsPbI$_3$; thus, TA results show similar behavior with pure CsPbI$_3$. The excited electrons then diffuse to the interface and transfer to C$_{60}$. That is why the reduction of TA bleaching signal for bilayer sample occurs after several ps.[51] On the other hand, for the illuminating direction from C$_{60}$ side (right), the excited position is close to the CsPbI$_3$/C$_{60}$ interface. Excited electrons, especially hot electrons, will rapidly transfer to hybrid states and LUMO of C$_{60}$. Therefore, at the very initial rising stage, TA can only detect the bleaching signal of cooled electrons. The disappearance of hot electrons' signal at the initial stage is highly consistent with 2PPE results of near resonance between CsPbI$_3$'s excited states and hybrid states.

We further explore the TA kinetics at the probe wavelength of 1200 nm, which is commonly regarded as the TA response of charge carriers.[11,52] As shown in Figure 5f, for pure CsPbI$_3$, the time constant for charge carriers' generation is ≈352 fs. After depositing with a C$_{60}$ layer, the rise of charge carriers is faster than pure CsPbI$_3$ with a time constant of ≈251 fs. As perovskite

and fullerene both have TA response of charge carriers at this IR region,[52,53] the sources of this signal may involve three sources, that is, 1) intrinsic charge carriers in CsPbI$_3$, 2) transferred electrons in C$_{60}$, and 3) remaining holes in CsPbI$_3$. Although we cannot judge their relative contributions, the earlier appearance of TA signal for CsPbI$_3$/C$_{60}$ bilayer is definitely due to the charge-transfer process. This result also verifies the ultra-short timescale of electron-transfer observed in 2PPE experiments.

3. Conclusion

Collection of charge carriers is one core factor influencing the performance of perovskite solar cell. In the conventional viewpoint, efficient charge collection requires a favorable energy-level alignment, which is an energy cascade for charge carriers from perovskite to CTL. The reduction of energy level in CTL; however, can lead to i) the energy loss for charge carriers and ii) non-radiative recombination due to back-transfer, making J_{SC} and V_{OC} a trade-off relationship. How to diminish V_{OC} loss due to the energy-level cascade; while, maintaining a high charge collection efficiency is a key issue for promoting efficiency of perovskite solar cells in future. The present in situ 2PPE experiments provide, for the first time, direct experimental observation of an ultrafast electron-transfer process overcoming the unfavorable energy-level alignment between perovskite and fullerene. Experiments and DFT calculations reveal that it is the electronic coupling that generates large numbers of interfacial hybrid states,

acting as a channel for electrons to extract from perovskite into fullerene. The measured transfer timescale is in the order of ≈100 fs, which is even comparable with the relaxation of hot electrons inside the conduction band and much faster than trap-induced and band-to-band recombination.

The established mechanism has important implications on the device design. It suggests a scenario that efficient charge collection can be accomplished even with a comparable or higher energy level in CTL, leading to an improved V_{OC} without sacrificing J_{SC}. The pathway to achieve this improvement is to construct interfacial hybrid states between perovskite and CTL. This requires synthesis of novel CTL materials that present strong electronic coupling with perovskite. Another key point for keeping efficient charge-transfer through unfavorable energy-level alignment is to improve charge carrier mobility. Take electron-transfer as an example, due to the energy cascade in LUMO/CBM of ETL and CBM of perovskite, electron back-transfer to CBM of perovskite is a major factor that limits the electron extraction efficiency. A high mobility can fast drive electrons toward cathode via diffusion or drift, avoiding electron accumulation at the perovskite/ETL interface and decreasing the back-transfer possibility. In addition, the charge accumulation at interfaces is also regarded as one origin for hysteresis in perovskite solar cells.[54,55] A high charge-transfer rate can avoid this drawback. This may also be a reason why previous perovskite solar cells in the p–i–n structure with fullerene as ETL show slight hysteresis. The methodology that improves electron-transfer rate via enhancing interfacial electronic coupling; thus, acts as a guideline for advanced design of perovskite solar cell.

4. Experimental Section

Sample Preparation: CsPbI$_3$, C$_{60}$ (Lumtec), and UGH-2 (Lumtec) films were prepared in a high vacuum condition (<10^{-8} mbar) by thermal-evaporation. Specifically, CsPbI$_3$ was prepared by co-evaporating two sources of CsI and PbI$_2$ (Xi'an Polymer Light Technology Corp) in the ratio of ≈1.5:1. The film was then annealed at 50 °C for 5 mins to form black phase. The black phase could preserve at vacuum condition even when the temperature returned to room temperature. The thickness of CsPbI$_3$ was 20 nm for all the characterizations.

Photoelectron Spectroscopy (PES): Ultraviolet and X-ray photoelectron spectroscopy were carried out in an ultra-high vacuum analysis chamber with base pressure ≈10^{10} Torr. The UV source was a He-discharge lamp producing He–I photons of 21.22 eV, and the X-ray source was a monochromatic Al–Kα X-ray gun with photon energy of 1486.6 eV. The photoelectron spectra were recorded with a hemispherical electron energy analyzer (Phoibos 150, SPECS). The samples for PES measurements were directly transferred into an analysis chamber after thermal evaporation without exposing to air.

Two-Photon Photoelectron Spectroscopy (2PPE): 2PPE experiments were carried out in the same chamber with photoelectron spectroscopy. In 2PPE, samples were first excited by a pump laser pulse with center photon energy of 1.88 eV (pulse energy ≈55 nJ, duration ≈30 fs) to generate electrons in conduction band of CsPbI$_3$. Then, the electrons were ionized by a probe beam with a photon energy of 4.68 eV (pulse energy ≈ 0.08 nJ, duration ≈ 20 fs) in a specific delay time. The kinetic energy of the ionized electrons was detected by the energy analyzer for calculating their electronic energy. The pump and probe laser pulses were generated by non-collinear optical parametric amplifiers (NOPA) of Orpheus-N-2H and 3H (Light Conversion), respectively. Both NOPAs were pumped by a fs laser (1030 nm, Light Conversion Pharos) running at frequency of 250 kHz. The

spot size of the pump beam was ≈2 mm^2. The samples were negatively biased at 6.8 V during measurement. The pulse durations of pump and probe lights were measured at the output ports of two NOPAs. The full width at half maximum (FWHM) of instrumental response function (IRF) was 0.13 ps. This broadening of IRF FWHM may be due to the optical components, such as lens, filters, and port glass of vacuum chamber, in 2PPE optical system.

Transient Absorption (TA): The samples for TA measurements were encapsulated in the glovebox with N$_2$ atmosphere after thermal evaporation, avoiding exposure to air. The visible TA experiment was performed with the laser of Pharos operating at 10 kHz and a TA100-DZ pump/probe setup (Time-Tech Spectra). The white-light continuum probe beam was generated by focusing the regenerative amplifier's fundamental 1030 nm laser pulses into a YAG crystal and collecting by a CMOS sensor. The pump beam (660 nm, ≈0.15 μJ cm^{-2}) was produced by the second harmonic output of Orpheus-N-2H. For the near infrared (NIR) region, the TA system used amplified Ti:sapphire fs laser (800 nm wavelength, 50 fs and 1 kHz repetition; Coherent Libra) and a Helios pump/probe setup (Ultrafast Systems). The NIR probe beam was generated by focusing the partial of the fundamental 800 nm beam onto a 1 cm sapphire crystal rod. The pump pulses were generated from an optical parametric amplifier (600 nm, 1.4 μJ cm^{-2}, Coherent TOPAS).

Material Characterizations: XRD patterns were measured using a D2 Phaser instrument with Cu Kα (λ = 0.154 nm) radiation source. Absorption spectra were recorded with Shimadzu 1700 model UV–vis spectroscopy. Steady-state and time-resolved PL spectra were measured with FLS980 fluorescence spectrometers (Edinburgh Instruments Ltd.). The excitation source for the steady-state PL was 400 nm monochromatic light from a Xe lamp with a power intensity of ≈0.85 mW cm^{-2}. For time-resolved PL, the excitation source was a ps pulse laser (Edinburgh Instruments, EPLED-560) with wavelength of 560 nm and fluence of ≈0.75 × 10^{-14} J cm^{-2}. The thickness of C$_{60}$ for absorption and PL was 20 nm. The atomic force microscope (AFM) was characterized with Hitachi 5300E. The samples for absorption and PL measurements were encapsulated in the glovebox to avoid exposing to air. For XRD and AFM, the fresh samples were moved to facilities immediately after they were taken out from the vacuum or glovebox to alleviate the influence of the atmosphere.

Computational Methods: The CsPbI$_3$ slab model was constructed with a (2 × 2) lateral periodicity and consisted of three octahedral layers of γ-phase CsPbI$_3$, featuring an exposed (100) surface. For the C$_{60}$/CsPbI$_3$ interfacial model, a C$_{60}$ molecule was placed on the top surface of CsPbI$_3$ (100), and the interfacial replicas were separated by ≈20 Å of vacuum. This structure was optimized at the gradient approximation/Perdew–Burke–Ernzerhof level using the PWSCF code, as implemented in the QUANTUM ESPRESSO package.[56] The ultrasoft pseudopotentials were employed, and uniform Brillouin zone grids of 6 × 6 × 4 k-mesh for CsPbI$_3$ bulk and 1 × 1 × 1 k-mesh for the C$_{60}$/CsPbI$_3$ interface were used. The cutoff of the plane-wave basis set was set at 25 Ry for wavefunctions and 200 Ry for charge density. The optimized crystal structure of C$_{60}$/CsPbI$_3$ interface was considered as the starting point for generating molecular dynamics trajectories, with the Andersen thermostat maintaining the system temperature at 300 K.

The nonadiabatic molecular dynamics (NAMD) simulations were conducted using the mixed quantum-classical fewest switching surface hopping (FSSH) technique, implemented within the framework of time-dependent Kohn–Sham density functional theory (TD-DFT). In this method, the lighter and faster electrons were treated quantum mechanically; while, the heavier and slower nuclei were described classically. However, it is worth noting that treating nuclei classically neglects the quantum effects such as zero-point energy and tunneling. In addition, the probability of surface hopping and the rates of nonadiabatic transitions were often based on approximations (i.e., Tully's fewest switches algorithm). Herein, NAMD simulations for the C$_{60}$/CsPbI$_3$ interface were performed using the PYXAID2 code.[57,58] The simulations began with the time-dependent Schrödinger equation $i\hbar \frac{\partial}{\partial t} \Psi_n (r, t) = H(r, R, t) \Psi_n(r, t)$, where $\hbar$ is the reduced Planck constant, $\Psi_n(r,t)$ are the wave functions

2407406 (8 of 10)

of the occupied single-electron Kohn-Sham orbitals, $H(r, R, t)$ is time-dependent Hamiltonian, r is the electronic coordinate, and R is nuclear coordinate. The NAMD simulations also involved Kohn–Sham orbitals $\Psi_n (r, t) = \sum_k C_k^n(t) \Phi_k(r; R(t))$, where $\Phi_k(r; R(t))$ are the adiabatic single-electron Kohn–Sham orbitals and $C_k^n(t)$ are the adiabatic states expansion coefficients. The probability of transition between adiabatic states i and j could be calculated using the wavefunction expansion coefficients and coupling defined as $d_{ij} = -i\hbar\Phi_i | \frac{\partial}{\partial t} | \Phi_j$.[57,58] Here, the focus was on studying the hot-electron cooling and transfer processes by calculating the average energy and population of hot electrons from excited state (CBM + 3) to CBM in $CsPbI_3$ and to hybrid state.

Statistical Analysis: The obtained 2PPE spectrum without background was got by subtracting a spectrum collected at negative delay times from the raw spectrum. The UPS spectra were fitted with Gaussian functions to obtained the crossover point with base lines. The global and target analysis of 2PPE were carried out using software of Glotaran. The 2PPE spectrum at particular delay time was fitted with Gaussian functions to identify the state's contributions.

Supporting Information

Supporting Information is available from the Wiley Online Library or from the author.

Conflict of Interest

The authors declare no conflict of interest.

Data Availability Statement

The data that support the findings of this study are available from the corresponding author upon reasonable request.

[1] J. Park, J. Kim, H.-S. Yun, M. J. Paik, E. Noh, H. J. Mun, M. G. Kim, T. J. Shin, S. I. Seo, *Nature* **2023**, *616*, 724.

[2] C. Luo, G. Zheng, F. Gao, X. Wang, C. Zhan, X. Gao, Q. Zhao, *Nat. Photonics* **2023**, *17*, 856.

[3] M. Li, R. Sun, J. Chang, J. Dong, Q. Tian, H. Wang, Z. Li, P. Yang, H. Shi, C. Yang, Z. Wu, R. Li, Y. Yang, A. Wang, S. Zhang, F. Wang, W. Huang, T. Qin, *Nat. Commun.* **2023**, *14*, 573.

[4] C. Ma, F. T. Eickemeyer, S.-H. Lee, D.-H. Kang, S. J. Kwon, M. Grätzel, N.-G. Park, *Science* **2023**, *379*, 173.

[5] S. Zhang, F. Ye, X. Wang, R. Chen, H. Zhang, L. Zhan, X. Jiang, Y. Li, X. Ji, S. Liu, M. Yu, F. Yu, Y. Zhang, R. Wu, Z. Liu, Z. Ning, D. Neher, L. Han, Y. Lin, H. Tian, W. Chen, M. Stolterfoht, L. Zhang, W.-H. Zhu, Y. Wu, *Science* **2023**, *380*, 404.

[6] T. Yang, L. Gao, J. Lu, C. Ma, Y. Du, P. Wang, Z. Ding, S. Wang, P. Xu, D. Liu, H. Li, X. Chang, J. Fang, W. Tian, Y. Yang, S. Liu, K. Zhao, *Nat. Commun.* **2023**, *14*, 839.

[7] Q. Jiang, X. Zhang, J. You, *Small* **2018**, *14*, 1801154.

[8] H. Min, D. Y. Lee, J. Kim, G. Kim, K. S. Lee, J. Kim, M. J. Paik, Y. K. Kim, K. S. Kim, M. G. Kim, T. J. Shin, S. I. Seok, *Nature* **2021**, *598*, 444.

[9] P. Caprioglio, J. A. Smith, R. D. J. Oliver, A. Dasgupta, S. Choudhary, M. D. Farrar, A. J. Ramadan, Y.-H. Lin, M. G. Christoforo, J. M. Ball, J. Diekmann, J. Thiesbrummel, K.-A. Zaininger, X. Shen, M. B. Johnston, D. Neher, M. Stolterfoht, H. J. Snaith, *Nat. Commun.* **2023**, *14*, 932.

[10] J. Warby, S. Shah, J. Thiesbrummel, E. Gutierrez-Partida, H. Lai, B. Alebachew, M. Grischek, F. Yang, F. Lang, S. Albrecht, F. Fu, D. Neher, M. Stolterfoht, *Adv. Energy Mater.* **2023**, *13*, 2303135.

[11] A. Marchioro, J. Teuscher, D. Friedrich, M. Kunst, R. van de Krol, T. Moehl, M. Grätzel, J.-E. Moser, *Nat. Photonics* **2014**, *8*, 250.

[12] R. A. Marcus, *J. Chem. Phys.* **1956**, *24*, 966.

[13] C. M. Wolff, F. Zu, A. Paulke, L. P. Toro, N. Koch, D. Neher, *Adv. Mater.* **2017**, *29*, 1700159.

[14] Q. Xue, Y. Bai, M. Liu, R. Xia, Z. Hu, Z. Chen, X.-F. Jiang, F. Huang, S. Yang, Y. Matsuo, H.-L. Yip, Y. Cao, *Adv. Energy Mater.* **2017**, *7*, 1602333.

[15] H. Hu, S. Moghadamzadeh, R. Azmi, Y. Li, M. Kaiser, J. C. Fischer, Q. Jin, J. Maibach, I. M. Hossain, U. W. Paetzold, B. A. Nejand, *Adv. Funct. Mater.* **2022**, *32*, 2107650.

[16] C. Ding, Y. Zhang, F. Liu, Y. Kitabatake, S. Hayase, T. Toyoda, K. Yoshino, K. Minemoto, K. Katayama, Q. Shen, *Nano Energy* **2018**, *53*, 17.

[17] R. Montecucco, E. Quadrivi, R. Po, G. Grancini, *Adv. Energy Mater.* **2021**, *11*, 2100672.

[18] Q. Zhao, A. Hazarika, L. T. Schelhas, J. Liu, E. A. Gaulding, G. Li, M. Zhang, M. F. Toney, P. C. Sercel, J. M. Luther, *ACS Energy Lett.* **2020**, *5*, 238.

[19] F. Ye, S. Zhang, J. Warby, J. Wu, E. Gutierrez-Partida, F. Lang, S. Shah, E. Saglamkaya, B. Sun, F. Zu, S. Shoaee, H. Wang, B. Stiller, D. Neher, W.-H. Zhu, Y. Wu, *Nat. Commun.* **2022**, *13*, 7454.

[20] H.-S. Lin, I. Jeon, R. Xiang, S. Seo, J.-W. Lee, C. Li, A. Pal, S. Manzhos, M. S. Goorsky, Y. Yang, S. Maruyama, Y. Matsuo, *ACS Appl. Mater. Interfaces* **2018**, *10*, 39590.

[21] M.-F. Lo, Z.-Q. Guan, T.-W. Ng, C.-Y. Chan, C.-S. Lee, *Adv. Funct. Mater.* **2015**, *25*, 1213.

[22] P. Schulz, D. Cahen, A. Kahn, *Chem. Rev.* **2019**, *119*, 3349.

[23] I. Gueye, Y. Shirai, D. B. Khadka, O. Seo, S. Hiroi, M. Yanagida, K. Miyano, O. Sakata, *ACS Appl. Mater. Interfaces* **2021**, *13*, 50481.

[24] C. Quarti, F. D. Angelis, D. Beljonne, *Chem. Mater.* **2017**, *29*, 958.

[25] J. Endres, D. A. Egger, M. Kulbak, R. A. Kerner, L. Zhao, S. H. Silver, G. Hodes, B. P. Rand, D. Cahen, L. Kronik, A. Kahn, *J. Phys. Chem. Lett.* **2016**, *7*, 2722.

[26] F. Zhang, J. C. Hamill, Y.-L. Loo, A. Kahn, *Adv. Mater.* **2020**, *32*, 2003482.

[27] X. Liu, E. Rezaee, H. Shan, J. Xu, Y. Zhang, Y. Feng, J. Dai, Z.-K. Chen, W. Huang, Z.-X. Xu, *J. Mater. Chem. C* **2018**, *6*, 4706.

[28] H. Choi, C.-K. Mai, H.-B. Kim, J. Jeong, S. Song, G. C. Bazan, J. Y. Kim, A. J. Heeger, *Nat. Commun.* **2015**, *6*, 7348.

[29] M. Liu, S. Dahlström, C. Ahläng, S. Wilken, A. Degterev, A. Matuhina, M. Hadadian, M. Markkanen, K. Aitola, A. Kamppinen, J. Deska, O. Mangs, M. Nyman, P. D. Lund, J.-H. Smått, R. Österbacka, P. Vivo, *J. Mater. Chem. A* **2022**, *10*, 11721.

**ADVANCED
SCIENCE NEWS**

www.advancedsciencenews.com

**ADVANCED
MATERIALS**

www.advmat.de

[30] Z. Guan, Y. Li, Z. Zhu, Z. Zeng, Z. Chen, Z. Ren, G. Li, S.-W. Tsang, H.-L. Yip, Y. Xiong, C.-S. Lee, *Adv. Funct. Mater.* **2022**, *32*, 2203962.

[31] W.-L. Chan, M. Ligges, A. Jailaubekov, L. Kaake, L. Miaja-Avila, X.-Y. Zhu, *Science* **2011**, *334*, 1541.

[32] T. Wang, T. R. Kafle, B. Kattel, W.-L. Chan, *J. Am. Chem. Soc.* **2017**, *139*, 4098.

[33] D. Niesner, H. Zhu, K. Miyata, P. P. Joshi, T. J. S. Evans, B. J. Kudisch, M. T. Trinh, M. Marks, X.-Y. Zhu, *J. Am. Chem. Soc.* **2016**, *138*, 15717.

[34] M. B. Price, J. Butkus, T. C. Jellicoe, A. Sadhanala, A. Briane, J. E. Halpert, K. Broch, J. M. Hodgkiss, R. H. Friend, F. Deschler, *Nat. Commun.* **2015**, *6*, 8420.

[35] A. A. Zhumekenov, M. I. Saidaminov, M. A. Haque, E. Alarousu, S. P. Sarmah, B. Murali, I. Dursun, X.-H. Miao, A. L. Abdelhady, T. Wu, O. F. Mohammed, O. M. Bakr, *ACS Energy Lett.* **2016**, *1*, 32.

[36] J. S. Manser, P. V. Kamat, *Nat. Photonics* **2014**, *8*, 737.

[37] G. Dutton, X.-Y. Zhu, *J. Phys. Chem. B* **2004**, *108*, 7788.

[38] A. E. Jailaubekov, A. P. Willard, J. R. Tritsch, W.-L. Chan, N. Sai, R. Gearba, L. G. Kaake, K. J. Williams, K. Leung, P. J. Rossky, X.-Y. Zhu, *Nat. Mater.* **2013**, *12*, 66.

[39] J. Xu, A. Buin, A. H. Ip, W. Li, O. Voznyy, R. Comin, M. Yuan, S. Jeon, Z. Ning, J. J. McDowell, P. Kanjanaboos, J.-P. Sun, X. Lan, L. N. Quan, D. H. Kim, I. G. Hill, P. Maksymovych, E. H. Sargent, *Nat. Commun.* **2015**, *6*, 7081.

[40] B. W. Caplins, D. E. Suich, A. J. Shearer, C. B. Harris, *J. Phys. Chem. Lett.* **2014**, *5*, 1679.

[41] G. Grancini, M. Maiuri, D. Fazzi, A. Petrozza, H.-J. Egelhaaf, D. Brida, G. Cerullo, G. Lanzani, *Nat. Mater.* **2013**, *12*, 29.

[42] T. Virgili, A. Calzolari, I. S. López, B. Vercelli, G. Zotti, A. Catellani, A. Ruini, F. Tassone, *J. Phys. Chem. C* **2013**, *117*, 5969.

[43] L. L. Kelly, D. A. Racke, H. Kim, P. Ndione, A. K. Sigdel, J. J. Berry, S. Graham, D. Nordlund, O. L. A. Monti, *Adv. Mater.* **2016**, *28*, 3960.

[44] P. J. Conaghan, S. M. Menke, A. S. Romanov, S. T. E. Jones, A. J. Pearson, E. W. Evans, M. Bochmann, N. C. Greenham, D. Credgington, *Adv. Mater.* **2018**, *30*, 1802285.

[45] J. Yin, R. Naphade, P. Maity, L. Gutiérrez-Arzaluz, D. Almalawi, I. S. Roqan, J.-L. Brédas, O. M. Bakr, O. F. Mohammed, *Nat. Commun.* **2021**, *12*, 3995.

[46] Y. Chen, J. Yin, Q. Wei, C. Wang, X. Wang, H. Ren, S. F. Yu, O. M. Bakr, O. F. Mohammed, M. Li, *Nat. Photonics* **2022**, *16*, 485.

[47] Q. Wei, H. Ren, J. Liu, Q. Liu, C. Wang, T. W. Lau, L. Zhou, T. Bian, Y. Zhou, P. Wang, Q. Lei, O. F. Mohammed, M. Li, J. Yin, *ACS Energy Lett.* **2023**, *8*, 3005.

[48] Q. Zhao, A. Hazarika, X. Chen, S. P. Harvey, B. W. Larson, G. R. Teeter, J. Liu, T. Song, C. Xiao, L. Shaw, M. Zhang, G. Li, M. C. Beard, J. M. Luther, *Nat. Commun.* **2019**, *10*, 2842.

[49] S. Narra, E. Jokar, O. Pearce, C.-Y. Lin, A. Fathi, E. W.-G. Diau, *J. Phys. Chem. Lett.* **2020**, *11*, 5699.

[50] M. Zhou, J. S. Sarmiento, C. Fei, H. Wang, *J. Phys. Chem. C* **2019**, *123*, 22095.

[51] H. P. Pasanen, P. Vivo, L. Canil, H. Hempel, T. Unold, A. Abate, N. V. Tkachenko, *J. Phys. Chem. Lett.* **2020**, *11*, 445.

[52] M. Li, S. Bhaumik, T. W. Goh, M. S. Kumar, N. Yantara, M. Grätzel, S. Mhaisalkar, N. Mathews, T. C. Sum, *Nat. Commun.* **2017**, *8*, 14350.

[53] P. C. Y. Chow, S. Albert-Seifried, S. Gélinas, R. H. Friend, *Adv. Mater.* **2014**, *26*, 4851.

[54] B. Wu, K. Fu, N. Yantara, G. Xing, S. Sun, T. C. Sum, N. Mathews, *Adv. Energy Mater.* **2015**, *5*, 1500829.

[55] T. Chen, Z. Sun, M. Liang, S. Xue, *Phys. Chem. Chem. Phys.* **2020**, *22*, 245.

[56] P. Giannozzi, S. Baroni, N. Bonini, M. Calandra, R. Car, C. Cavazzoni, D. Ceresoli, G. L. Chiarotti, M. Cococcioni, I. Dabo, A. Dal Corso, S. de Gironcoli, S. Fabris, G. Fratesi, R. Gebauer, U. Gerstmann, C. Gougoussis, A. Kokalj, M. Lazzeri, L. Martin-Samos, N. Marzari, F. Mauri, R. Mazzarello, S. Paolini, A. Pasquarello, L. Paulatto, C. Sbraccia, S. Scandolo, G. Sclauzero, A. P. Seitsonen, et al., *J. Phys.: Condens. Matter* **2009**, *21*, 395502.

[57] A. V. Akimov, O. V. Prezhdo, *J. Chem. Theory Comput.* **2013**, *9*, 4959.

[58] A. V. Akimov, O. V. Prezhdo, *J. Chem. Theory Comput.* **2014**, *10*, 789.